


Magnetocrystalline anisotropy and exchange probed by high-field anomalous Hall effect in fully compensated half-metallic $\text{Mn}_2\text{Ru}_x\text{Ga}$ thin films

Ciarán Fowley,^{1,*} Karsten Rode,² Yong-Chang Lau,² Naganivetha Thiyagarajah,² Davide Betto,² Kiril Borisov,² Gwenaél Atcheson,² Erik Kampert,³ Zhaosheng Wang,^{3,†} Ye Yuan,¹ Shengqiang Zhou,¹ Jürgen Lindner,¹ Plamen Stamenov,² J. M. D. Coey,² and Alina Maria Deac¹

¹*Institute of Ion Beam Physics and Materials Research, Helmholtz-Zentrum Dresden - Rossendorf, Bautzner Landstraße 400, 01328 Dresden, Germany*

²*AMBER and School of Physics, Trinity College Dublin, Dublin 2, Ireland*

³*Hochfeld-Magnetlabor Dresden (HLD-EMFL), Helmholtz-Zentrum Dresden - Rossendorf, Bautzner Landstraße 400, 01328 Dresden, Germany*

 (Received 18 May 2018; revised manuscript received 24 October 2018; published 12 December 2018)

Magnetotransport is investigated in thin films of the half-metallic ferrimagnet $\text{Mn}_2\text{Ru}_x\text{Ga}$ in pulsed magnetic fields of up to 58 T. A nonvanishing Hall signal is observed over a broad temperature range, spanning the compensation temperature (155 K), where the net magnetic moment is strictly zero, the anomalous Hall conductivity is $6673 \Omega^{-1} \text{m}^{-1}$, and the coercivity exceeds 9 T. Molecular field modeling is used to determine the intra- and intersublattice exchange constants, and from the spin-flop transition we infer the anisotropy of the electrically active sublattice to be 216 kJ m^{-3} and predict the magnetic resonance frequencies. Exchange and anisotropy are comparable and hard-axis applied magnetic fields result in a tilting of the magnetic moments from their collinear ground state. Our analysis is applicable to collinear ferrimagnetic half-metal systems.

DOI: [10.1103/PhysRevB.98.220406](https://doi.org/10.1103/PhysRevB.98.220406)

Thin films with ultrahigh magnetic anisotropy fields exhibit magnetic resonances in the range of hundreds of GHz [1–3] which is promising for future telecommunications applications. Spin-transfer-driven nano-oscillators (STNOs), working on the principle of angular momentum transfer from a spin-polarized current to a small magnetic element [4,5], have achieved output powers of several μW and frequency tunabilities of $\sim\text{GHz mA}^{-1}$ [6,7], useful for wireless data transmission [8]. Output frequencies of STNOs based on standard transition-metal-based ferromagnets, such as CoFeB, or cubic Heusler alloys such as $\text{Co}_2\text{Fe}_{0.4}\text{Mn}_{0.6}\text{Si}$ are in the low GHz range [9–13].

Certain Heusler alloys [14,15] are a suitable choice for achieving much higher output frequencies, aimed at enabling communication networks beyond 5G [16]. The Mn_{3-x}Ga family contains two Mn sublattices which are antiferromagnetically coupled in a ferrimagnetic structure [14]. They have low net magnetization, M_{net} , and high effective magnetic anisotropy, K_{eff} , with anisotropy fields of $\mu_0 H_K = 2K_{\text{eff}}/M_{\text{net}}$ exceeding 18 T [17,18], which results in resonance frequencies two orders of magnitude higher [1,2] than CoFeB. Furthermore, the magnetic properties of these ferrimagnetic alloys can be tuned easily with composition [19–21]. Mn_{3-x}Ga films have shown tunable resonance frequencies between 200 and 360 GHz by variation of the alloy stoichiometry and magnetic anisotropy field [2].

Here, we focus on the fully compensated half-metallic Heusler compound $\text{Mn}_2\text{Ru}_x\text{Ga}$ (MRG) [20–25]. Films of MRG were first shown experimentally [20] and subsequently confirmed by density functional theory (DFT) calculations [25] to exhibit a spin gap at E_F . The material crystallizes in the cubic space group $F\bar{4}3m$. Mn on the $4a$ and $4c$ sites are antiferromagnetically coupled, while those on the same sites are ferromagnetically coupled. The crystal structure is shown in Fig. 1(a). The Ga is on the $4b$ sites and Ru occupies a fraction of the $4d$ sites [20]. We will discuss Mn on the $4a$ and $4c$ sites by referring to the Mn_{4a} and Mn_{4c} sublattices. By changing the Ru concentration, the magnetic properties of the Mn_{4c} sublattice are altered, while those of the Mn_{4a} sublattice remain relatively stable [21]. Thin films grown on MgO have an out-of-plane magnetic easy axis due to biaxial strain induced by the substrate during growth [23]. Unlike the uncompensated tetragonal $D0_{22}$ Mn_{3-x}Ga family of alloys, MRG has a compensation temperature, T_{comp} , where there is no net magnetization [20,21]. Nonetheless, there is nonvanishing tunnel magnetoresistance [22], spin Hall angle [23], and magneto-optical Kerr effect [24], which all arise from the Mn_{4c} sublattice. The occupied electronic states originating from the Mn_{4a} sublattice lie below the spin gap [25].

The electrical transport on MRG reported to date [22,23] can be explained using the model shown in Figs. 1(b) and 1(c) where the direction of spin polarization is governed by the direction of the Mn_{4c} sublattice and not Mn_{4a} or M_{net} . Here, we make use of the dominant influence of a single sublattice on the electron transport to study the magnetism of a compensated half metal at compensation, and evaluate the exchange and anisotropy energies.

*Corresponding author: c.fowley@hzdr.de

†Present address: High Magnetic Field Laboratory, Chinese Academy of Sciences, Hefei, Anhui 230031, People's Republic of China.

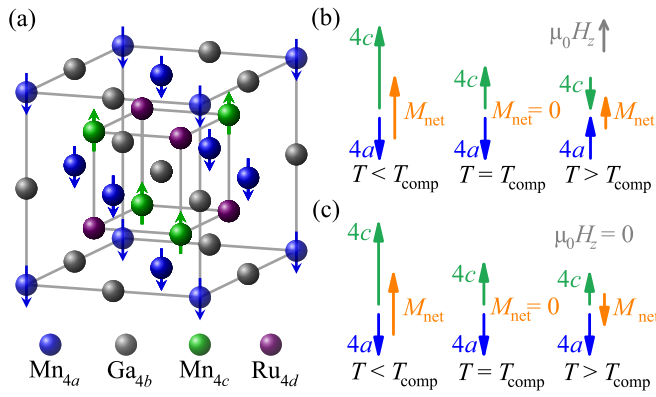


FIG. 1. (a) Crystal structure of Mn₂Ru_xGa: The magnetic moments of the Mn_{4a} and Mn_{4c} are aligned antiparallel. (b) and (c) A two-sublattice macrospin model used to explain the observed temperature and field dependences of electronic transport in the presence and absence of an applied field $\mu_0 H_z$, respectively. Two key points of the model are as follows: Below (above) T_{comp} the moment of the Mn_{4c} is parallel (antiparallel) to M_{net} , and, in the absence of an applied field, the sublattice moments do not change their orientation upon crossing T_{comp} .

We measure magnetotransport, especially the anomalous Hall effect in the temperature range 10–300 K in magnetic fields up to 58 T. The anomalous Hall conductivity (AHC) of a metallic ferromagnetic film, σ_{xy} , is proportional to the out-of-plane component of magnetization M_z , which is defined as $M \cos \theta$ where θ is the angle between the z axis and the magnetization M [26]. In ferrimagnets, however, the AHC will depend on the band structure at the Fermi level E_F , so when the material is half-metallic, one expects $\sigma_{xy} \propto M_{\text{sl}} \cos \theta_{M_{\text{sl}}}$, where M_{sl} is the magnetization of the sublattice that dominates the transport.

Mn₂Ru_xGa layers of varying composition, $x = 0.55, 0.61, \text{ and } 0.70$, were deposited on MgO substrates in a fully automated Shamrock sputtering system. The thickness of the films, ≈ 27 nm, was determined by x-ray reflectivity. Hall crosses of width 100 μm and length 900 μm were patterned using direct-laser-write lithography, Ar⁺ ion milling, and lift-off. The Hall bars were contacted with Cr 5 nm/Au 125 nm pads.

A Lakeshore Hall system was used to measure the longitudinal (ρ_{xx}) and transverse (ρ_{xy}) resistivities from 10 to 300 K in out-of-plane fields up to 6.5 T. The AHC, $\sigma_{xy} = \rho_{xy}/\rho_{xx}^2$ [27,28], is obtained from the raw data. In-plane, $\mu_0 H_x$, and out-of-plane, $\mu_0 H_z$, pulsed magnetic fields of up to 58 T were applied at the Dresden High Magnetic Field Laboratory at selected temperatures between 10 and 220 K. We focus on Mn₂Ru_{0.61}Ga with $T_{\text{comp}} \approx 155$ K. All three compositions were found to have compensation temperatures between 100 and 300 K, and exhibit similar properties.

AHC loops versus $\mu_0 H_z$ around T_{comp} are shown in Fig. 2(a). At all temperatures, MRG exhibits strong perpendicular magnetic anisotropy. The reversal of the sign of σ_{xy} between 135 and 165 K indicates a reversal of the spin polarization at E_F with respect to the applied field direction, as expected on crossing T_{comp} . The coercivity, $\mu_0 H_c$, varies from 3 to 6 T between 110 and 175 K. The longitudinal magnetore-

sistance, $\rho_{xx}(H)/\rho_{xx}(0)$, shown in Fig. 2(b) is small ($< 1\%$), as expected for a half metal [29]. Pulsed field measurements in Fig. 2(c) show that, close to T_{comp} , $\mu_0 H_c$ exceeds 9 T and that MRG exhibits a spin-flop transition at higher fields, indicated in the figure by the gray arrows. The derivative of selected curves of σ_{xy} versus applied field [Fig. 2(d)] shows up the spin-flop field, especially at lower temperatures. We note that the longitudinal magnetoresistance up to 58 T also does not exceed 1% (not shown). The divergence in coercivity [black circles in Fig. 2(e)] is expected at T_{comp} because the anisotropy field in uniaxial magnets is $\mu_0 H_K = 2K_{\text{eff}}/M_{\text{net}}$, where K_{eff} is the effective anisotropy energy and M_{net} is the net magnetization. The anisotropy field is an upper limit on coercivity. The temperature dependence of the spin-flop field, $\mu_0 H_{\text{sf}}$, is also plotted in Fig. 2(e) (red squares).

The solid (dashed) line in Fig. 2(f) traces the temperature dependence of σ_{xy} when the sample is initially saturated in a field of -6.5 T ($+6.5$ T) at 10 K and allowed to warm up in zero applied magnetic field. The spontaneous Hall conductivity σ_{xy} decreases from 7859 to 5290 $\Omega^{-1} \text{m}^{-1}$ and does not change sign for either of the zero-field temperature scans. The remanent value of σ_{xy} after the application of 6.5 T (58 T) is plotted with open (solid) symbols. The combined data establish that, in MRG films, neither the anomalous Hall effect (AHE) nor the AHC are proportional to M_{net} . They depend on the magnetization of the sublattice that gives rise to σ_{xy} . While similar behavior is well documented for the anomalous Hall effect in rare-earth–transition-metal (RE-TM) ferrimagnets, where both RE and TM elements contribute to the transport [30–32], in MRG both magnetic sublattices are composed of Mn which has been confirmed to have the same electronic configuration, $3d^5$ [21]. If both sublattices contributed equally to the effect, the sum should fall to zero at T_{comp} .

We refer to the model presented in Figs. 1(b) and 1(c) to explain the behavior shown in Fig. 2(f). Figure 1(b) shows the Mn_{4a} and Mn_{4c} sublattice moments and the net magnetic moment in the case of an applied field $\mu_0 H_z$ along the easy axis of MRG. Below T_{comp} , the Mn_{4c} moment (green arrow) outweighs that of Mn_{4a} (blue arrow), and M_{net} (orange arrow) is parallel to the Mn_{4c} sublattice. At T_{comp} , M_{net} is zero but the directions of the sublattice moments have not changed with respect to $\mu_0 H_z$. Above T_{comp} , $\mu_0 H_z$ causes a reversal of M_{net} (provided it exceeds $\mu_0 H_c$). Here, the Mn_{4a} sublattice has a larger moment than Mn_{4c} and M_{net} will be in the same direction as the Mn_{4a} moment. Due to the antiferromagnetic alignment of both sublattices the moment on Mn_{4c} is parallel (antiparallel) to $\mu_0 H_z$ below (above) T_{comp} .

In the absence of an applied field [Fig. 1(c)], the direction of M_{net} will reverse on crossing T_{comp} due to the different temperature dependences of the sublattice moments. However, the net sublattice moments only change in magnitude, and not direction. The uniaxial anisotropy provided by the slight substrate-induced distortion of the cubic cell [20] provides directional stability along the z axis. Therefore, crossing T_{comp} in the absence of applied field, we expect no change in the sign of σ_{xy} , nor should it vanish. The Mn_{4c} sublattice dominates the electron transport and determines the spin direction of the available states at E_F , while the Mn_{4a} states form the spin gap.

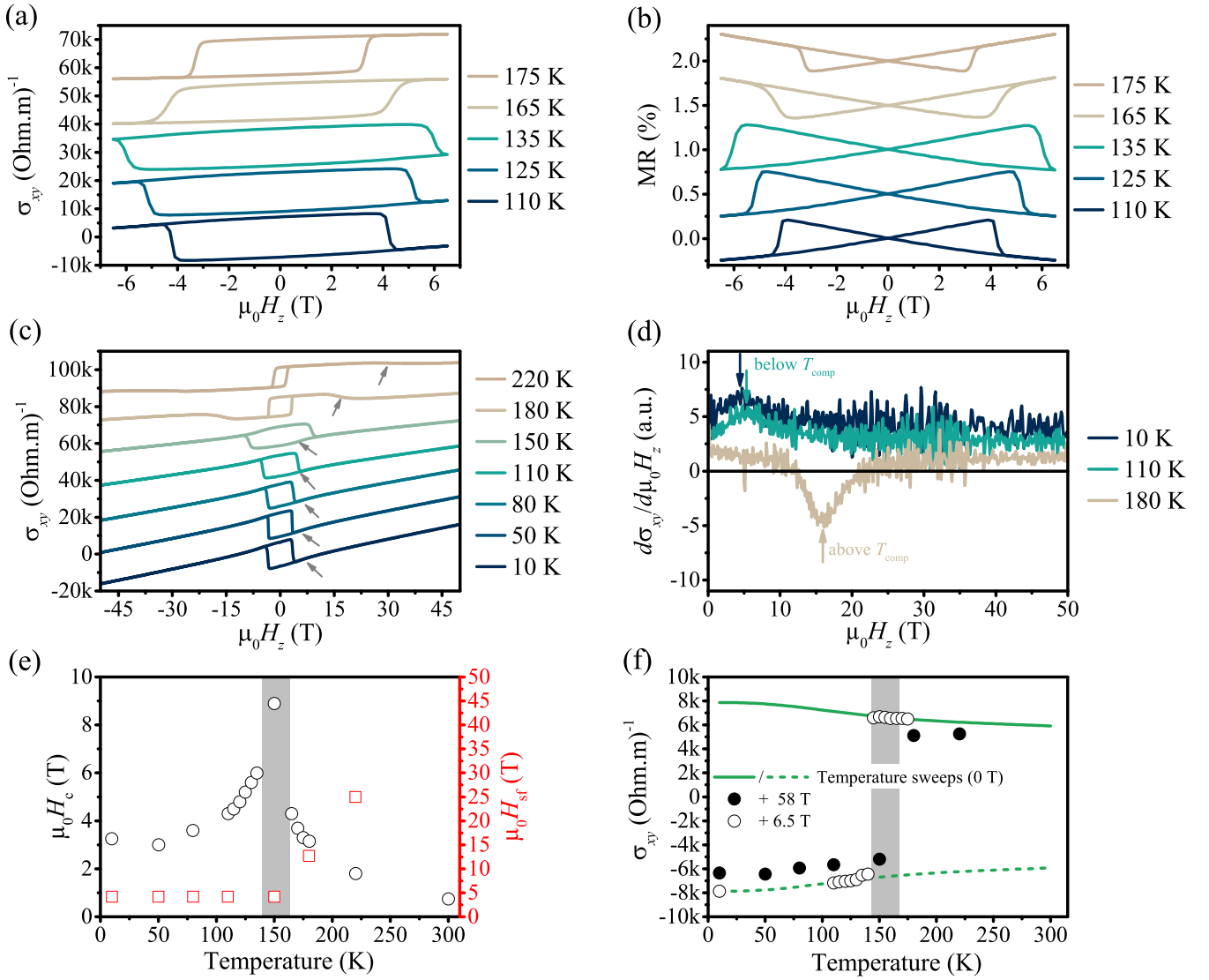


FIG. 2. (a) AHC loops up to 6.5 T for $\text{Mn}_2\text{Ru}_{0.61}\text{Ga}$ around the compensation temperature (155 K). Loops are offset vertically for clarity. (b) Magnetoresistance loops recorded at the same time as the data in (a). Loops are offset vertically for clarity. (c) AHC loops up to 58 T, where the spin-flop transition is indicated by the grey arrows. The linear slope is due to the ordinary Hall effect. Loops are offset vertically for clarity. (d) Derivative of the selected data in (c) clearly highlighting the spin flop. (e) $\mu_0 H_c$ (black circles) and $\mu_0 H_{sf}$ (red squares) as a function of temperature. The divergence of the coercivity is expected at T_{comp} since $M_{\text{net}} = 0$ and $K_{\text{eff}} \neq 0$. (f) Temperature dependence of the remanent Hall conductivity when saturated at 10 K in negative (solid line) and positive (dashed line) applied field. The black open (solid) circles record the remanent Hall resistivity after the application of 6.5 T (58 T).

The results of a molecular field model [33] based on two sublattices are presented in Fig. 3. The molecular field H^i experienced by each sublattice is given by

$$H_{4a}^i = n_{4a-4a}M_{4a} + n_{4a-4c}M_{4c} + H, \quad (1)$$

$$H_{4c}^i = n_{4a-4c}M_{4a} + n_{4c-4c}M_{4c} + H, \quad (2)$$

where n_{4a-4a} and n_{4c-4c} are the intralayer exchange constants and n_{4a-4c} is the interlayer exchange constant. M_{4a} and M_{4c} are the magnetizations of the 4a and 4c sublattices. H is the externally applied magnetic field. The moments within the Mn_{4a} and Mn_{4c} sublattices are ferromagnetically coupled and hence n_{4a-4a} and n_{4c-4c} are both positive. The two sublattices couple antiferromagnetically and therefore n_{4a-4c} is negative.

The equations are solved numerically for both temperature and applied field dependences to obtain the projection of both sublattice magnetizations along the z axis, $M_{z-\alpha} = M_{\alpha} \cos \theta_{\alpha}$, where $\alpha = 4a, 4c$. In the absence of an applied field, $\theta = 0$, therefore $M_{z-\alpha}$ reduces simply to M_{α} .

The model parameters are given in Table I. Based on previous x-ray magnetic circular dichroism (XMCD) measurements [21] as well as DFT calculations [25] we take values of 547 and 585 kA m^{-1} for the magnetizations on the 4a and 4c sublattice, respectively. The values of n_{4a-4a} , n_{4c-4c} , and n_{4a-4c} are fitted to reproduce T_{comp} and the Curie temperature, T_C . The temperature dependences of M_{z-4a} (blue line), M_{z-4c} (green line), and M_{net} (orange line) with $n_{4a-4a} = 1150$, $n_{4c-4c} = 400$, and $n_{4a-4c} = -485$ are shown in Fig. 3(a). In order to numerically obtain the temperature dependence in

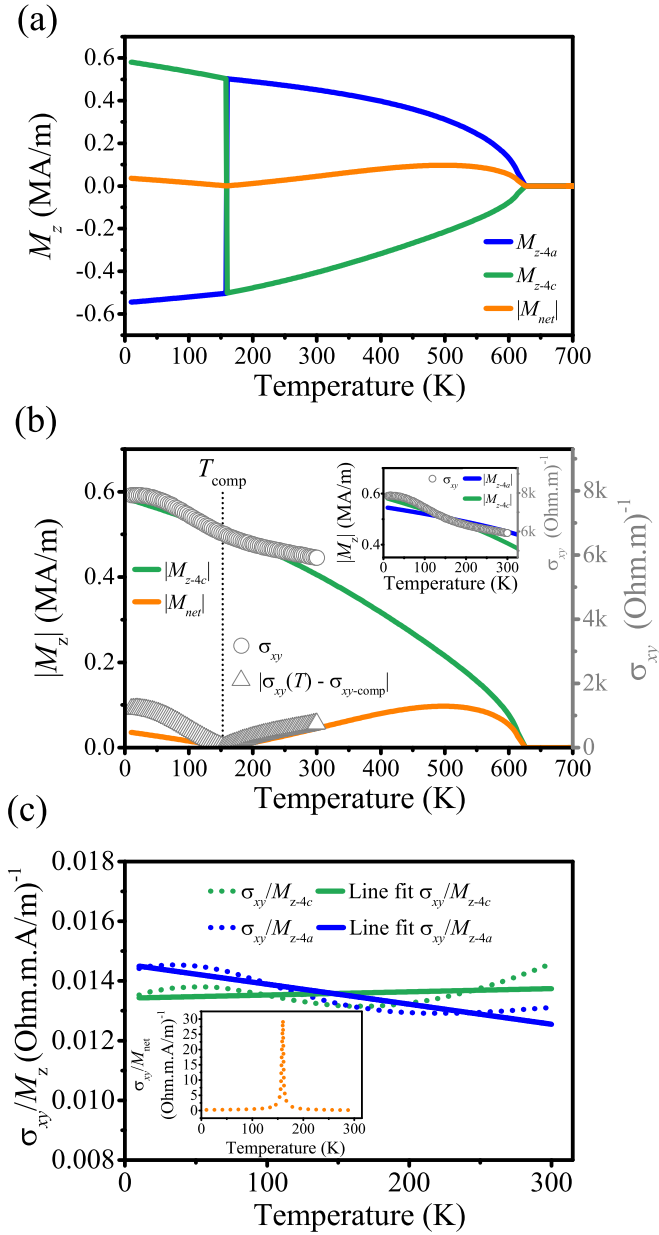


FIG. 3. (a) Temperature dependence of M_{z-4a} and M_{z-4c} and M_{net} . The data are obtained from numerical integration with an applied field to set the direction of the net magnetization and then reduced to zero, therefore the magnetization reverses at T_{comp} . T_{comp} is 155 K and the Curie temperature is 625 K. (b) σ_{xy} , $|\sigma_{xy}(T) - \sigma_{xy-comp}|$, $|M_{z-4c}|$, and $|M_{net}|$ as a function of temperature. Inset: σ_{xy} plotted with M_{z-4a} and M_{z-4c} as a function of temperature, to show that σ_{xy} does indeed follow M_{z-4c} and not M_{z-4a} . (c) Ratio of σ_{xy}/M_{z-4c} and σ_{xy}/M_{z-4a} (dotted lines) over the experimentally measured temperature range complete with linear fits (solid lines). The ratio is almost constant with no significant linear background slope showing that $\sigma_{xy} \propto M_{z-4c}$. The inset shows the clear divergence of σ_{xy}/M_{net} at T_{comp} .

zero applied field, a strong field of 60 T is used to set the direction of M_{net} and then reduced to zero, so the sublattice moments reverse at $T_{comp} = 155$ K as in the experiment. T_C is

TABLE I. Initial parameters input to the molecular field model according to Eqs. (1) and (2). M_{4a} , M_{4c} and K_{4a} , K_{4c} are the magnetizations and uniaxial anisotropies on the 4a, 4c sublattices. n_{4a-4a} and n_{4c-4c} are the intralayer exchange constants. n_{4a-4c} is the interlayer exchange constant. Derived parameters are outputs of the molecular field model.

Initial parameters			
M_{4a} (0 K)	547 kA m ⁻¹	n_{4a-4a}	1150
M_{4c} (0 K)	585 kA m ⁻¹	n_{4c-4c}	400
K_{4a}	0 kJ m ⁻³	n_{4a-4c}	-485
K_{4c}	216 kJ m ⁻³		
Derived parameters			
M_{net} (10 K)	38 kA m ⁻¹	T_C	625 K
M_{net} (max.)	97 kA m ⁻¹	T_{comp}	155 K

625 K. M_{net} varies from 38 kA m⁻¹ at 10 K to a maximum of 97 kA m⁻¹ at 512 K, close to T_C .

Figure 3(b) shows the measured AHC (circles), along with $|M_{z-4c}|$ (green line) from the molecular field model. It can be seen clearly that σ_{xy} follows the temperature dependence of M_{z-4c} below T_{comp} and not M_{net} . As a further step, we plot $|M_{net}|$ from the molecular field model (orange line) with $|\sigma_{xy}(T) - \sigma_{xy-comp}|$ (triangles). As σ_{xy} is proportional only to M_{4c} and at compensation $M_{4c} = M_{4a}$, subtracting the value of σ_{xy} at T_{comp} ($|\sigma_{xy}(T) - \sigma_{xy-comp}|$) gives an approximate indication of how M_{net} behaves with temperature. Even though this ignores the weak M_{4a} temperature dependence, the trend of M_{net} follows $|\sigma_{xy}(T) - \sigma_{xy-comp}|$, showing that σ_{xy} is a reflection of M_{4c} and not M_{net} . The inset in Fig. 3(b) shows both M_{z-4a} and M_{z-4c} with the experimentally obtained σ_{xy} , and shows that σ_{xy} more closely follows M_{z-4c} . The relative decrease of M_{z-4c} from 10 to 300 K, $\sim 40\%$, is more than double that of M_{z-4a} , in line with previously reported XMCD measurements [21]. Figure 3(c) shows the ratio of σ_{xy} to M_{z-4c} (green dotted line), M_{z-4a} (blue dotted line), and M_{net} (inset). Linear fitting of σ_{xy}/M_{z-4c} (solid green line) and σ_{xy}/M_{z-4a} (solid blue line) shows that σ_{xy}/M_{z-4c} remains constant over the measured temperature range, and is equal to $0.0136 \Omega^{-1} \text{m}^{-1} \text{A}^{-1} \text{m}$, similar to what has been reported for other itinerant ferromagnetic systems [34,35]. The linear slope for σ_{xy}/M_{z-4a} and the divergence of σ_{xy}/M_{net} shows that σ_{xy} reflects neither of these two quantities.

A recent study has shown via *ab initio* calculations that this must be the case for a fully compensated half-metallic ferrimagnetic system [36], although previous reports on bulk films found ρ_{xy} , and hence σ_{xy} , falling to zero at T_{comp} [37].

For the evaluation of the magnetic anisotropy we use the initial low-field change of σ_{xy} vs $\mu_0 H_x$ and extrapolate to zero and obtain K_{4c} (not shown). The values obtained vary from 100 to 250 kJ m⁻³ over the entire data range. We also calculate the anisotropy directly from the spin-flop transition $H_{sf} = \sqrt{2H_K H_{4c}^{ex}}$, where H_K is the sublattice anisotropy field and H_{4c}^{ex} is the exchange field, the first term in Eq. (2). The anisotropy field H_K is related to the sublattice anisotropy energy K_{4c} .

A comparison between the experiment and the model at 220 K for both $\mu_0 H_z$ and $\mu_0 H_x$ is shown in Fig. 4. The

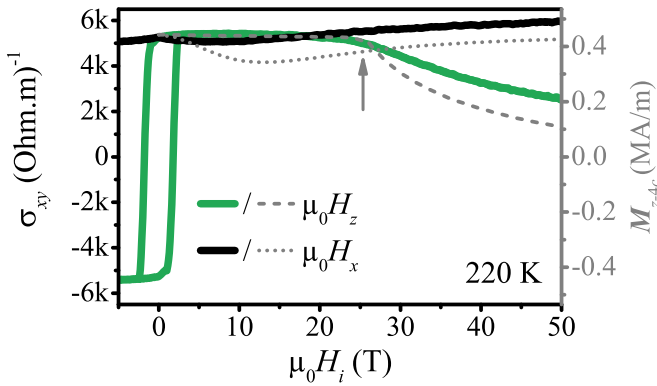


FIG. 4. Comparison of experimental data (solid lines) and molecular field model (dashed lines) at 220 K for fields applied along $\mu_0 H_z$ and $\mu_0 H_x$. $\mu_0 H_{sf}$ is observed in both cases at 26 T, marked by the gray arrow.

solid lines plot the experimentally obtained σ_{xy} , while the dashed lines plot M_{z-4c} from the model. The spin-flop field is observed in both cases at $\mu_0 H_z = 26$ T. For the case of $\mu_0 H_x$, it can first be seen that the $4c$ moment does not saturate along the field as one would expect [18,38]. It initially decreases but then returns to a saturated value in both the experimental data and the model. This behavior is due to the fact that in MRG the exchange and anisotropy energies are comparable and weak. If the exchange coupling is strong, then the net magnetic moment could be saturated along $\mu_0 H_x$ as both sublattices can remain antiparallel up to the anisotropy field $\mu_0 H_K = 2(K_{4a} + K_{4c})/(M_{4a} + M_{4c}) = 2K_{\text{eff}}/M_{\text{net}}$. If the exchange coupling is weak, then both sublattice moments will tilt from their antiparallel alignment, breaking exchange, before the net magnetic moment can be saturated along $\mu_0 H_x$ at the appropriate sublattice anisotropy field $\mu_0 H_K = 2K_{sl}/M_{sl}$, $sl = 4a, 4c$.

The model and experiment disagree slightly on the temperature dependence of H_{sf} below T_{comp} . Better agreement can be obtained by using much higher anisotropy energies of opposite sign: $K_{4a} = -1.5 \text{ MJ m}^{-3}$ and $K_{4c} = 1.7 \text{ MJ m}^{-3}$.

This has the effect of increasing (decreasing) H_{sf} above (below) T_{comp} . While this improves the match between σ_{xy} vs $\mu_0 H_z$ below T_{comp} , it worsens the match of σ_{xy} vs $\mu_0 H_x$ at all temperatures. This and the slight discrepancies between the model and experiment when a low value of K_{4c} is used (Fig. 4) indicate that additional anisotropies, likely cubic, in MRG, as well as antisymmetric exchange (Dzyaloshinskii-Moriya interaction) should be taken into account.

We have shown that the uniaxial molecular field model reproduces the main characteristics of the experimental data and we confirm the relationship $\sigma_{xy} \propto M_{4c} \cos \theta_{M_{4c}}$. Knowing H_K and H_{4c}^{ex} we can predict the frequencies of the anisotropy, $f_{\text{anis}} = \gamma \mu_0 H_K$, and the exchange, $f_{\text{exch}} = \gamma \mu_0 \sqrt{2H_K H_{4c}^{\text{ex}}} = \gamma \mu_0 H_{sf}$, magnetic resonance modes, where $\gamma = 28.02 \text{ GHz T}^{-1}$ [39]. At 220 K, $\mu_0 H_{sf} = 26$ T and $\mu_0 H_{4c}^{\text{ex}} = n_{4a-4c} M_{4a} = 294$ T, therefore $\mu_0 H_K = 1.15$ T and the resonances are $f_{\text{anis}} = 32$ GHz and $f_{\text{exch}} = 729$ GHz.

In conclusion, σ_{xy} for fully compensated half-metallic ferrimagnetic alloys follows the relevant sublattice magnetization $M_{sl} \cos \theta_{M_{sl}}$ and not $M_{\text{net}} \cos \theta_{M_{\text{net}}}$. High-field magnetotransport and molecular field modeling allows the determination of the anisotropy and exchange constants provided the half-metallic material is collinear. $\text{Mn}_2\text{Ru}_x\text{Ga}$ behaves magnetically as an antiferromagnet and electrically as a highly spin-polarized ferromagnet; It is capable of operation in the THz regime and its transport behavior is governed by the Mn_{4c} sublattice. The immediate, technologically relevant, implication of these results is that spin-transfer torque effects in compensated ferrimagnetic half metals will be governed by a single sublattice.

ACKNOWLEDGMENTS

This project has received funding from the European Union's Horizon 2020 research and innovation programme under Grant Agreement No. 737038 (TRANSPiRE). This work is supported by the Helmholtz Young Investigator Initiative Grant No. VH-N6-1048. We acknowledge the support of the HLD at HZDR, member of the European Magnetic Field Laboratory (EMFL).

- [1] S. Mizukami, F. Wu, A. Sakuma, J. Walowski, D. Watanabe, T. Kubota, X. Zhang, H. Naganuma, M. Oogane, Y. Ando, and T. Miyazaki, *Phys. Rev. Lett.* **106**, 117201 (2011).
- [2] N. Awari, S. Kovalev, C. Fowley, K. Rode, R. Gallardo, Y.-C. Lau, D. Betto, N. Thiyagarajah, B. Green, O. Yildirim, J. Lindner, J. Fassbender, J. Coey, A. Deac, and M. Gensch, *Appl. Phys. Lett.* **109**, 032403 (2016).
- [3] S. Mizukami, S. Iihama, Y. Sasaki, A. Sugihara, R. Ranjbar, and K. Suzuki, *J. Appl. Phys.* **120**, 142102 (2016).
- [4] J. Slonczewski, *J. Magn. Magn. Mater.* **159**, L1 (1996).
- [5] L. Berger, *Phys. Rev. B* **54**, 9353 (1996).
- [6] A. Deac, A. Fukushima, H. Kubota, H. Maehara, Y. Suzuki, S. Yuasa, Y. Nagamine, K. Tsunekawa, D. Djayaprawira, and N. Watanabe, *Nat. Phys.* **4**, 803 (2008).
- [7] S. Ikeda, J. Hayakawa, Y. Ashizawa, Y. Lee, K. Miura, H. Hasegawa, M. Tsunoda, F. Matsukura, and H. Ohno, *Appl. Phys. Lett.* **93**, 082508 (2008).
- [8] H. Choi, S. Kang, S. Cho, I.-Y. Oh, M. Shin, H. Park, C. Jang, B.-C. Min, S.-I. Kim, S.-Y. Park, and C. Park, *Sci. Rep.* **4**, 5486 (2014).
- [9] S. Ikeda, K. Miura, H. Yamamoto, K. Mizunuma, H. Gan, M. Endo, S. Kanai, J. Hayakawa, F. Matsukura, and H. Ohno, *Nat. Mater.* **9**, 721 (2010).
- [10] W. H. Rippard, A. M. Deac, M. R. Pufall, J. M. Shaw, M. W. Keller, S. E. Russek, G. E. W. Bauer, and C. Serpico, *Phys. Rev. B* **81**, 014426 (2010).
- [11] W. Skowronski, T. Stobiecki, J. Wrona, G. Reiss, and S. van Dijken, *Appl. Phys. Express* **5**, 063005 (2012).

- [12] Z. Zeng, G. Finocchio, B. Zhang, P. Amiri, J. Katine, I. Krivorotov, Y. Huai, J. Langer, B. Azzaroni, K. Wang, and H. Jiang, *Sci. Rep.* **3**, 1426 (2013).
- [13] T. Yamamoto, T. Seki, T. Kubota, H. Yako, and K. Takanashi, *Appl. Phys. Lett.* **106**, 092406 (2015).
- [14] T. Graf, C. Felser, and S. Parkin, *Prog. Solid State Chem.* **39**, 1 (2011).
- [15] Q. Ma, T. Kubota, S. Mizukami, X. Zhang, H. Naganuma, M. Oogane, Y. Ando, and T. Miyazaki, *Appl. Phys. Lett.* **101**, 032402 (2012).
- [16] S. Dhillon, M. Vitiello, E. Linfield, A. Davies, M. Hoffmann, J. Booske, C. Paoloni, M. Gensch, P. Weightman, G. Williams, E. Castro-Camus, D. Cumming, F. Simoens, I. Escorcia-Carranza, J. Grant, S. Lucyszyn, M. Kuwata-Gonokami, K. Konishi, M. Koch, C. Schmuttenmaer *et al.*, *J. Phys. D* **50**, 043001 (2017).
- [17] H. Kurt, K. Rode, M. Venkatesan, P. Stamenov, and J. M. D. Coey, *Phys. Status Solidi B* **248**, 2338 (2011).
- [18] C. Fowley, S. Ouardi, T. Kubota, O. Yildirim, A. Neudert, K. Lenz, V. Sluka, J. Lindner, J. Law, S. Mizukami, G. Fecher, C. Felser, and A. M. Deac, *J. Phys. D* **48**, 164006 (2015).
- [19] M. Glas, D. Ebke, I. M. Imort, P. Thomas, and G. Reiss, *J. Magn. Magn. Mater.* **333**, 134 (2013).
- [20] H. Kurt, K. Rode, P. Stamenov, M. Venkatesan, Y. C. Lau, E. Fonda, and J. M. D. Coey, *Phys. Rev. Lett.* **112**, 027201 (2014).
- [21] D. Betto, N. Thiyagarajah, Y. C. Lau, C. Piamonteze, M. A. Arrio, P. Stamenov, J. M. D. Coey, and K. Rode, *Phys. Rev. B* **91**, 094410 (2015).
- [22] K. Borisov, D. Betto, Y. C. Lau, C. Fowley, A. Titova, N. Thiyagarajah, G. Atcheson, J. Lindner, A. M. Deac, J. M. D. Coey, P. Stamenov, and K. Rode, *Appl. Phys. Lett.* **108**, 192407 (2016).
- [23] N. Thiyagarajah, Y. C. Lau, D. Betto, K. Borisov, J. M. D. Coey, P. Stamenov, and K. Rode, *Appl. Phys. Lett.* **106**, 122402 (2015).
- [24] K. Fleischer, N. Thiyagarajah, Y.-C. Lau, D. Betto, K. Borisov, C. C. Smith, I. V. Shvets, J. M. D. Coey, and K. Rode, *Phys. Rev. B* **98**, 134445 (2018).
- [25] M. Žic, K. Rode, N. Thiyagarajah, Y.-C. Lau, D. Betto, J. M. D. Coey, S. Sanvito, K. J. O’Shea, C. A. Ferguson, D. A. MacLaren, and T. Archer, *Phys. Rev. B* **93**, 140202(R) (2016).
- [26] N. Nagaosa, J. Sinova, S. Onoda, A. MacDonald, and N. Ong, *Rev. Mod. Phys.* **82**, 1539 (2010).
- [27] C. Zeng, Y. Yao, Q. Niu, and H. H. Weitering, *Phys. Rev. Lett.* **96**, 037204 (2006).
- [28] W. L. Lee, S. Watauchi, V. L. Miller, R. J. Cava, and N. P. Ong, *Science* **303**, 1647 (2004).
- [29] F. J. Yang, Y. Sakuraba, S. Kokado, Y. Kota, A. Sakuma, and K. Takanashi, *Phys. Rev. B* **86**, 020409 (2012).
- [30] A. Ogawa, T. Katayama, M. Hirano, and T. Tsushima, *Jpn. J. Appl. Phys.* **15**, 87 (1976).
- [31] Y. Mimura, N. Imamura, and Y. Kushiuro, *J. Appl. Phys.* **47**, 3371 (1976).
- [32] T. McGuire, R. Gambino, and R. Taylor, *J. Appl. Phys.* **48**, 2965 (1977).
- [33] J. S. Smart, *Effective Field Theories of Magnetism* (Saunders, Philadelphia, 1966).
- [34] N. Manyala, Y. Sidis, J. Ditsa, G. Aeppli, D. Young, and Z. Fisk, *Nat. Mater.* **3**, 255 (2004); cited By 137.
- [35] A. Husmann and L. J. Singh, *Phys. Rev. B* **73**, 172417 (2006).
- [36] R. Stinshoff, S. Wimmer, H. Ebert, G. H. Fecher, C. Felser, and S. Chadov, *arXiv:1710.04453*.
- [37] R. Stinshoff, G. Fecher, S. Chadov, A. Nayak, B. Balke, S. Ouardi, T. Nakamura, and C. Felser, *AIP Adv.* **7**, 105009 (2017).
- [38] V. Guo, B. Lu, X. Wu, G. Ju, B. Valcu, and D. Weller, *J. Appl. Phys.* **99**, 08E918 (2006).
- [39] A. H. Morrish, *Physical Principles of Magnetism* (Wiley, New York, 1965), Chap. 10, pp. 539–639.